AN ANALYSIS OF NANOINDENTATION IN ELASTO-PLASTIC SOLIDS

B. POON[1], D. RITTEL[2] and G. RAVICHANDRAN[1*]

[1]Graduate Aeronautical Laboratories, California Institute of Technology Pasadena, CA 91125, U.S.A

[2] Faculty of Mechanical Engineering, Technion, 32000 Haifa, Israel

Keywords: A. indentation, B. elastic plastic solids, C. elastic modulus, D. mechanics, E. finite elements

ABSTRACT

This paper examines the accuracy of the extracted elastic properties using the nanoindentation technique on elasto-plastic materials. The application of the correction factor evaluated in the linearly elastic case (Poon, *et al.*, 2008) on elastic-plastic materials is critically examined. It is then established that the accurate determination of the projected area of contact is found to be crucial for the accurate determination of elastic material properties. The conventional methods for the accurate determination of contact area are generally limited to ratios of Young's modulus over yield stress, $E/\sigma_y < 30$ for elastic-perfectly plastic materials, which is too stringent for most materials. Thus, a new electrical resistance method is proposed to measure directly the projected contact area. Using numerical simulations, it was found that with the accurate determination of A, the error associated with the extracted elastic material properties is reduced by more than 50% in some cases. Using the newly proposed procedure, the error is also found to be independent of E/σ_y and the tip radius, ρ, and it is only a function of Poisson's ratio, ν. This suggests that the errors might be due to the residual stresses at the plastic imprint that were found to depend on ν as well.

* Author to whom correspondence should be addressed. E-mail: ravi@caltech.edu

1. INTRODUCTION

Nanoindentation has been an increasingly popular technique for material characterization in the nanoscale. Developed in the early 1970s (Bulychev, *et al.*, 1975; Loubet, *et al.*, 1984; Newey, *et al.*, 1982; Pethica, *et al.*, 1983; Ternovskii, *et al.*, 1974), commercial nanoindenters have since been developed, and this technology is widely available for researchers interested in thin films and small volumes as motivated by modern applications, e.g. microelectronics, MEMS etc.

Nanoindentation was originally developed to measure the elastic properties of the material of interest (Bulychev, *et al.*, 1975; Pharr, *et al.*, 1992). With the advent of better technology, researchers have since developed novel applications, such as acoustic emission testing (Shiwa, *et al.*, 1996; Tymiak, *et al.*, 2003), impact testing (Fischer-Cripps, 2004), fracture toughness testing (Lawn, *et al.*, 1980; Palmqvist, 1957), constant strain rate/creep testing (Bower, *et al.*, 1993; Mayo and Nix, 1988; Storåkers and Larsson, 1994), high temperature testing (Atkins and Tabor, 1966; Kutty, *et al*., 1996; Payzant, *et al.*, 1993) and most recently *in situ* electrical measurement testing (Mann, *et al.*, 2002; Ruffell, *et al.*, 2007) for the nanoindenter.

The basic determination of the material elastic properties is most often a requirement for further determination of additional mechanical properties. While the first paper (Poon, *et al.*, 2008) considered purely elastic materials to establish some basic facts and correlations, it is evident that the overwhelming majority of materials display plastic flow to some extent during the nanoindentation process. This inevitably deviates from the linear elastic assumptions on which Sneddon's derivation is based. However, the main assumption underlying all nanoindentation experiments, is that while the loading stage is elastic-plastic, the unloading stage is purely elastic, and thus is quite suitable for elastic analyses. The elastic unloading assumption is based on the validity of the following two components:

a. the unloading-subsequent reloading load-displacement curves coincide;
b. the reloading of a residual imprint can be described as the indentation of a flat surface with an equivalent (thus different) indenter.

Moreover, the factors identified as relevant to linear elastic indentations, such as finite tip radius effect and radial displacement recovery, that are not considered in Sneddon's formulation (1948), might be pertinent towards elastic-plastic indentations as well. Thus, it is important to assess their relevance in the context of the indentation of isotropic, elastic-plastic materials, particularly, to examine the validity of the application of the correction factor derived for the linear elastic indentations (Hay, *et al.*, 1999; Poon, *et al.*, 2008; Troyon and Huang, 2004), in elastic-plastic indentations.

This paper critically reassesses the various assumptions used in extracting the linearly elastic material properties in an elastic-plastic indentation using experiments and numerical finite element calculations. In addition, the paper proposes viable methods to minimize theses errors and obtain an optimal estimation of the elastic and plastic properties. The conventional procedure for extracting the reduced modulus in elastic-plastic indentation is briefly reviewed in section 2. The results obtained through numerical simulations, the validity of the underlying assumptions and factors affecting the accuracy of the extracted material properties are all presented in section 3. A novel technique to directly measure the projected contact area is described in section 4. Experimental results from nanoindentation on elastic-plastic solids are used to illustrate the application of the suggested techniques for accurate evaluation of material properties. A summary and conclusions of the study are presented in section 5.

2. CONVENTIONAL EXTRACTION OF ELASTIC PROPERTIES

Figure 1(a) is a schematic of an indentation of an infinitely sharp conical indenter on an elastic-plastic specimen. The thick black line illustrates the indenter tip at its maximum depth, while the thick broken grey line illustrates the indenter tip when fully unloaded. Figure 1(b) plots the corresponding load-displacement curve for the indentation. The unloading is assumed to be elastic and h_e is the recoverable elastic displacement. Upon unloading, the reloading path is expected to follow that of the unloading until h_{max}, the maximum indentation depth of the previous indentation, is reached.

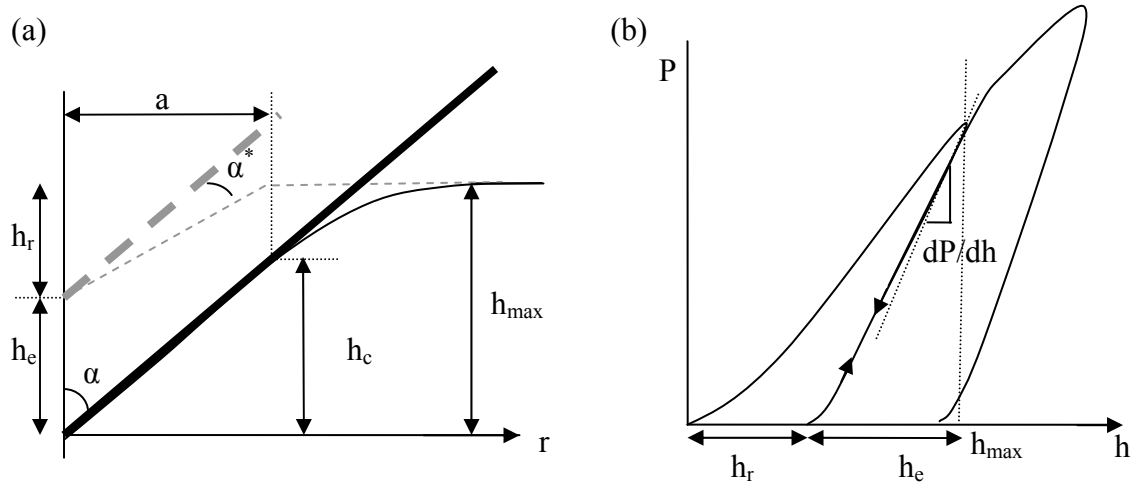

Fig. 1. (a) Schematic of an indentation at full load and unload; (b) The corresponding load-displacement curve. (After Fischer-Cripps, 2004).

The elastic unloading path can thus be described by the elastic load-displacement relations derived by Sneddon (1948) assuming an indentation of a rigid conical indenter on a linearly elastic half-plane, see also (Fischer-Cripps, 2004; Sakai, 2003),

$$P = \frac{2E\tan\alpha'}{\pi(1-\nu^2)} h_e^{\,2} \qquad (1)$$

where P is the load measured by the indenter, E and v are the Young's modulus and Poisson's ratio of the specimen, α' is the effective half angle of the indenter, and h_e is the recoverable elastic displacement of the indenter.

Although the reloading path is elastic and follows the previous unloading path until h_{max}, it is different from the case of elastic indentation derived by Sneddon (1948). Sneddon assumed that the conical tip is indenting a *flat elastic plane*, whereas during reloading, the conical tip is indenting on a residual imprint. Therefore, the effective half angle, α' is introduced, which takes into account α, the half angle of the conical indenter and also the residual imprint left from the previous indentation, as shown in Fig. 2.

Thus,

$$\alpha' = \frac{\pi}{2} - \alpha^* \tag{2}$$

where α^* is the angle between the indenter and the residual imprint.

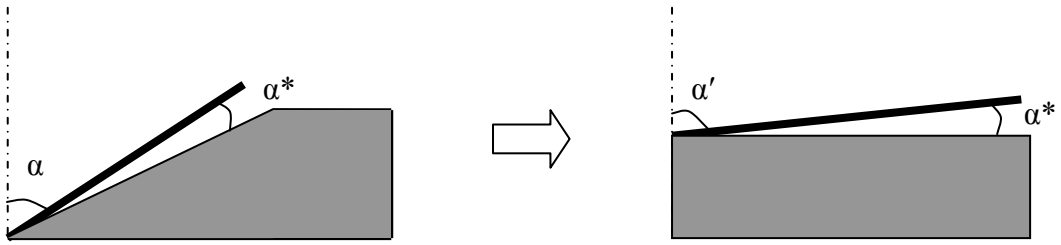

Fig. 2. Illustration of the equivalent indentation problem

Using a physical argument that the normal component of the stress at the surface of the specimen remain finite around the contact area with the tip, and an assumption that both the shear and normal stresses remain zero at the unperturbed surface, Sneddon (Fischer-Cripps, 2004; Sneddon, 1948) found that,

$$h = \left(\frac{\pi}{2} - \frac{r}{a}\right) a \cot\alpha' \qquad r \le a \tag{3}$$

Thus,

$$h_e = \frac{\pi}{2} a \cot \alpha' \tag{4}$$

Differentiating (1),

$$\frac{dP}{dh_e} = \frac{4E \tan \alpha'}{\pi(1-\nu^2)} h_e \tag{5}$$

Substituting (4) into (5),

$$\frac{E}{1-\nu^2} = \frac{1}{2\beta} \frac{dP}{dh_e} \frac{\sqrt{\pi}}{\sqrt{A}} \tag{6}$$

where A is the projected contact area. The left-hand side of (6) is the reduced modulus, E_r. In order to reassess the application of Sneddon's equation to nanoindentations, subsequent derivation of E_r is performed with $\beta = 1$.

The conventional relationship used in the extraction of elastic constants in depth-sensing indentation experiments is shown in (6). Bulychev *et al.* (1975) showed that (6) holds for cylindrical punch and spherical indenters. Subsequently, Pharr *et al.* (1992) showed that the relationship is true for all indenters that are bodies of revolution. For a Berkovich/Vickers equivalent cone ($\alpha = 70.3^o$), the projected contact area, A is given by,

$$A = \pi \tan^2 \alpha \, h_c^{\,2} = 24.5 h_c^{\,2} \tag{7}$$

where h_c is the contact depth. Note that, the projected contact area, A is calculated using the half-angle of the indenter, α. Using (1) and (3),

$$h_c = h_{\max} - \chi \frac{P|_{h_{\max}}}{dP/dh_e|_{h_{\max}}} \tag{8}$$

Note that $\chi \approx 0.72$ for conical indenters, and $\chi = 0.75$ for spherical indenters. Researchers have also proposed that χ is a function of the exponent of the unloading curve for the elastic-plastic

indentation (Martin and Troyon, 2002; Pharr and Bolshakov, 2002). With the load and displacement of the indenter monitored throughout the indentation, h_c and A can be calculated. The value of A can then be plugged into (6) to derive E_r for the material of interest. The accuracy of the conventional method is evaluated in the next section by means of numerical simulations.

3. NUMERICAL SIMULATION

Numerical 'experiments' were performed using commercial numerical finite element package, ABAQUS. The indentation experiment was modeled as a 2D axisymmetric problem using a total of 6252 three-node linear axisymmetric triangular elements (CAX3) for the specimen with converged geometry, i.e., r_s/h_s equals unity and h_s/h_{max} equals 100, where r_s, h_s and h_{max} are the radius and thickness of the specimen and maximum indentation depth respectively. A more refined mesh by doubling the number of elements was used for each specimen size but did not yield significantly different results (< 1% difference for the range of indentation depth of interest) for each simulation, which suggests convergence of the existing mesh. The mesh is denser at the indentation site and less dense away from the indentation to minimize computational time. The indenter was modeled as a rigid conical tip with a tip radius, ρ of 30 *nm* and 150 *nm*. The cylindrical specimen had a converged geometry (Poon, *et al.*, 2008), and was modeled as an isotropic, deformable elastic, perfectly plastic material, whose E/σ_y ranged from 10 to 1000, and v ranged from 0.01 to 0.47. The results of the numerical simulations are tabulated in Tables 1-4 in the Appendix.

3.1 The effective half angle α'

It is important to examine the relationship between α' and the mechanical properties of the indented material, as this will provide a relevant range of α' for typical materials. Figure 3 shows the relationship between the effective half-angle, α' and E/σ_y. For the linearly elastic case, α' is equivalent to the half-angle of the indenter, α (in this case 70.3^o). As E/σ_y becomes large, i.e., when plasticity becomes dominant, α' is observed to tend towards 90^o. This is consistent with the expectation that when the region of contact is completely plastic, there will be no elastic recovery and thus, the residual imprint will take the shape of the indenter upon unloading, so that α^* (Fig. 2) is 0^o, corresponding to α' of 90^o.

The theoretical cohesive strength, σ_c of a solid, is on the order of *E/10*. However, it is well documented that this is much larger than the typical strength of solids, which is typically between *E/100* and *E/1000*. Based on this estimate, the relevant α' for typical materials ranges between 88^o and 89.7^o. It should be noted that elastic, perfectly plastic materials considered here are the limiting case; materials that harden will reduce the extent of plasticity in the specimen under indentation and thus, reduce the effective half-angle, α' of the equivalent problem.

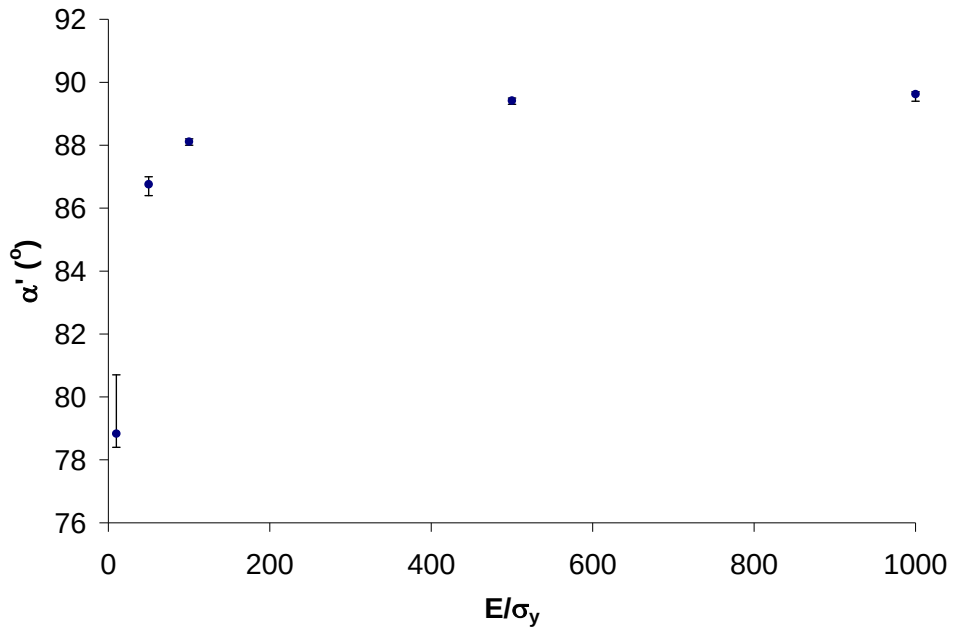

Fig. 3. Effective half-angle, α' vs. E/σ_y. Error bars represent spread of data for ν from 0.01 to 0.47.

3.2. The relationship between h_e/h_{max} and E/σ_y for elastic, perfectly plastic materials

The yield stress, σ_y of a rigid perfectly plastic material has been identified to be related to the hardness of the material through (Hill, *et al.*, 1947; Tabor, 1948; 1951)

$$H = C\,\sigma_y \tag{9}$$

For metals in general, it has been shown empirically that the constraint factor, $C \approx 3$. It would seem that with an accurate measurement of H, σ_y can be calculated in a straightforward manner, however, C is dependent on material properties namely, the extent of plasticity measured by E/σ_y, strain hardening, n and other strengthening mechanisms such as pressure sensitivity (in polymers and granular materials) etc. (Fischer-Cripps, 2004; Tabor, 1951). As such, C commonly varies from 1.5 – 3 and is largely material dependent. The relationship proposed subsequently in this section takes the extent of plasticity, E/σ_y into account. While the derived value of hardness depends on the actual contact area which is affected by effects of pile-ups and sink-ins (Miyake, *et al.*, 2004), the proposed relation uses the elastic recoverable displacement, h_e and maximum

indentation depth, h_{max}, to infer the value of the yield stress. These parameters are directly measured during an indentation experiment. For elastic, perfectly plastic solids, the proposed model takes pile-ups around the indentation into consideration by establishing a relationship between h_e and h_{max} with respect to E/σ_y. For hardening elastic plastic solids, the proposed model does not take sinks-ins around the indentation into consideration, thus provides an upper bound for σ_y.

Using numerical simulations, a relationship is identified between E/σ_y and h_e/h_{max}, which is given by,

$$\frac{h_e}{h_{\max}} = 2.98\left(\frac{E}{\sigma_y}\right)^{-0.68} . \qquad (10)$$

The relationship is obtained through the fitting of mean h_e/h_{max} at five discrete values of E/σ_y. The fit has a R^2 value of 0.999. The spread illustrated by the error bounds at each E/σ_y represents the range of values for ν ranging between 0.01 and 0.47 and for ρ ranging between 30 *nm* and 150 *nm*. The average standard deviation for each spread is approximately 12% of their respective mean.

The yield stress, σ_y can now be calculated for elastic, perfectly plastic materials using (10), since both h_e/h_{max} (Fig. 1) and E are typically measured or extracted from a typical indentation experiment. For hardening materials, the calculated σ_y using (10) is the upper bound for the actual σ_y. Elastic materials correspond to h_e/h_{max} of one. Materials that strain or pressure harden fall within the shaded area between h_e/h_{max} of one and the line given by (10).

The relation provided by (10) was verified in a series on nanoindentation experiments of single crystal aluminum oriented in the (100) direction, fused quartz, platinum based based bulk metallic glass, homalite (a brittle glassy polymer) and single crystal silicon oriented in the (100).

Their measured h_e/h_{max} ratios are plotted against the known ratio E/σ_y, as shown in Fig. 4. The experiments were carried out on a Hysitron^{TM} Triboindenter, with a Berkovich diamond tip. The load-displacement displacement curves were obtained following conventional correction techniques for machine compliance and other system calibrations such as thermal drift.

The first observation is that the data points for all materials fall within the shaded region, confirming that (10) is indeed a bound for elastic-plastic materials. The single crystal aluminum data fall on the elastic, perfectly plastic line, which suggests that this material does not significantly strain harden under confined flow during indentation. However, it should be noted that while h_e and h_{max} were measured directly from the nanoindentation experiments, bulk polycrystalline aluminum values for E and σ_y were used to determine the location on the x-axis. Due to the lack of grain boundaries, σ_y for single crystal aluminum is likely to be smaller than that for polycrystalline aluminum, which will shift the experimental points to the right into the shaded region. The single crystal aluminum was identified as highly anisotropic (Hansen and Huang, 1998), thus the selection of representative E and σ_y is non-trivial. Nonetheless, the use of bulk polycrystalline aluminum's properties provides some comparison for single crystal aluminum to other materials. Moreover, since the σ_y chosen is likely to overestimate the actual value of σ_y for single crystal aluminum, these experimental points provide a stringent confirmation that (10) is indeed a bound for elastic-plastic materials. The other materials were found to deviate from the elastic, perfectly plastic line, which can be attributed to the operation of hardening mechanisms, such as work hardening or hardening due to the high hydrostatic pressure created under the indenter tip. The statistical variations for the experiments are summarized in Table 5 in the Appendix.

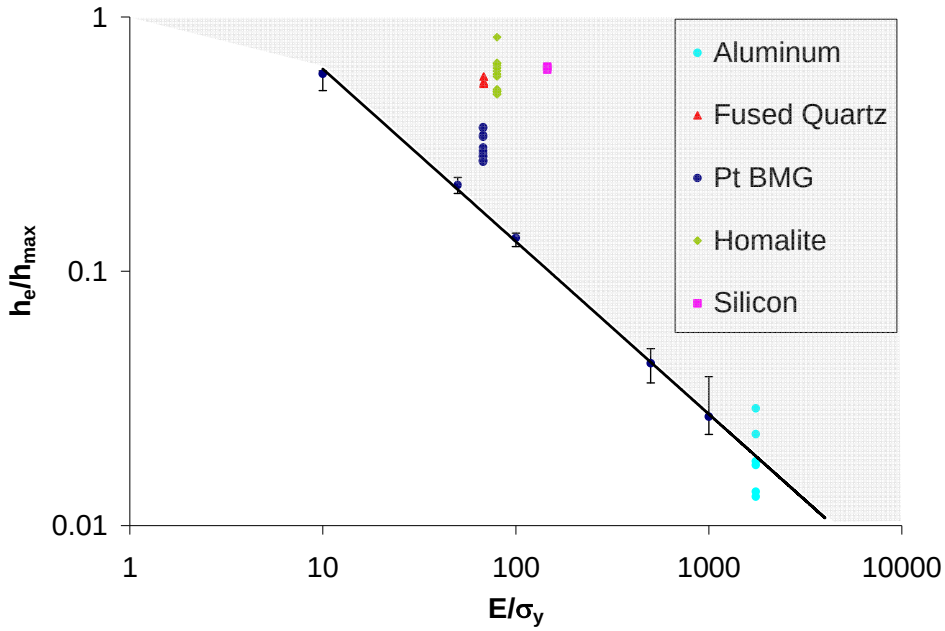

Fig. 4. E/σ_y vs. h_e/h_{max} for different materials.

3.3 Error involved in the conventional derivation

The percentage error, ε in the determination of elastic modulus E is defined as,

$$\varepsilon = \frac{E_{calculated} - E_{prescribed}}{E_{prescribed}} \cdot 100 \,. \tag{11}$$

The percentage error, ε is found to vary with ρ, ν and E/σ_y. From Tables 1 and 3, one can observe that ε is directly related to indenter tip radius, ρ, i.e. the use of a blunt tip results in a larger error using the conventional derivation.

The sensitivity of ε to changes in ν and E/σ_y can be seen from Fig. 5. It is observed that ε is larger as ν approaches 0. The percentage error on the extracted Young's modulus, E was also observed to increase with E/σ_y, i.e., the larger the extent of plasticity, the larger the error observed in the calculated E. This observation seems to imply the inaccuracy of the underlying elastic unloading assumption, which is central to the correctness of the conventional method. The elastic unloading

assumption is based on the two assumptions listed in the introduction section 1. These two assumptions are critically examined in the subsequent section.

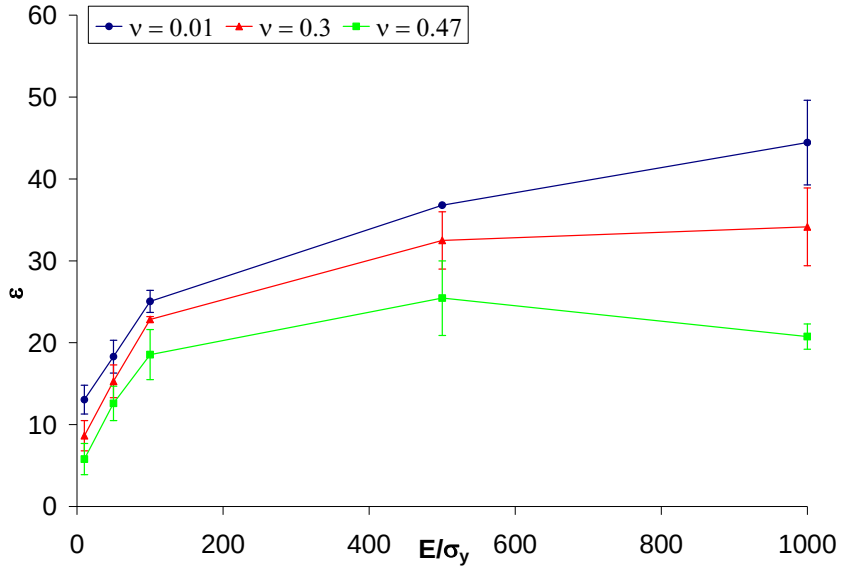

Fig. 5. Percentage error of E, ε vs. E/σ_y, for different ν (0.01, 0.3, 0.47). The spread represents different indenter tip radius ranging between 30 *nm* and 150 *nm*.

3.3 Examination of the underlying assumptions

3.3.1 Does the unloading and subsequent reloading load-displacement follow the same path?

The conventional derivation assumes that the unloading is elastic with the expectation that reloading of the indenter will take the prior unloading path until the prior maximum indentation depth, h_{max} is reached. To verify this assumption, indentation experiments and simulations were performed. Single crystal aluminum in the (100) orientation and fused quartz were indented with the Hysitron^{TM} Triboindenter. The experiments were carried out in a load-control mode, using a diamond Berkovich indenter tip. The specimens were indented to a preset load, then unloaded and reloaded to a higher preset load before the final unloading. A similar numerical 'experiment' was also performed using ABAQUS. The conical indenter tip was modeled as rigid with α =

70.3° and $\rho = 30\ nm$. The elastic, perfectly plastic cylindrical specimen was modeled with $E = 200\ GPa$, $\sigma_y = 1\ GPa$ and $v = 0.3$.

From Fig. 6, it can be observed that the unloading and reloading paths coincide for both the curves obtained through experiments and numerical simulation. The material properties of the specimens considered were varied and the extent of plasticity in the specimens during indentation was different. Thus, it can be concluded that the unloading curve is indeed elastic and the common assumption for the unloading path to be perceived as an elastic reloading path is valid.

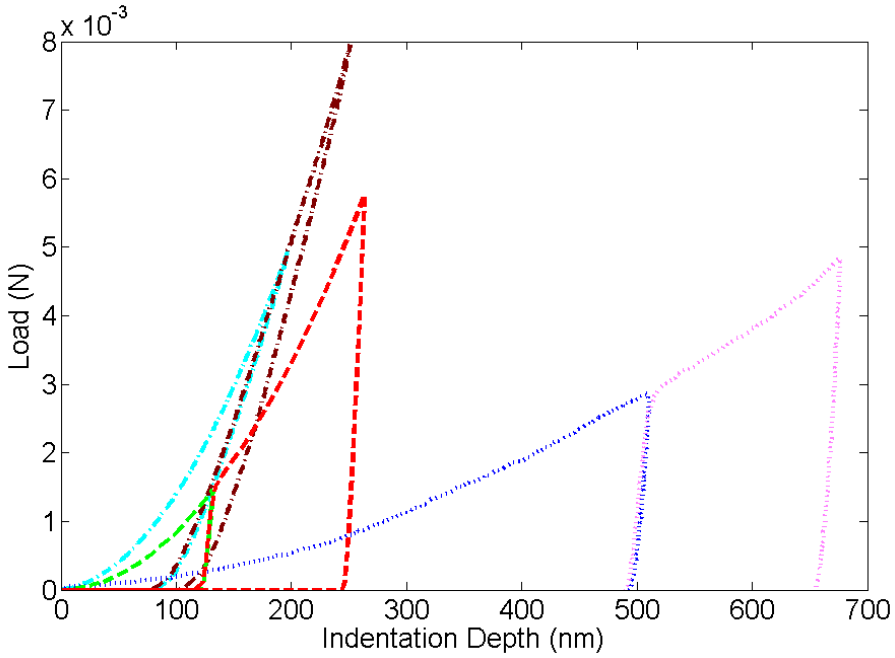

Fig. 6. Loading-reloading curves obtained from nanoindentation experiments on fused quartz (dash-dotted line) and single crystal aluminum (dotted line), and from numerical simulation with $E = 200\ GPa$, $\sigma_y = 1\ GPa$, $v = 0.3$ and $\rho = 30\ nm$ (dashed line).

3.3.2 Validity of the 'equivalent' problem

Having validated the assumption that the elastic unloading curve of the elastic-plastic indentation may be treated as an elastic loading curve of an indentation on a specimen with a

plastic imprint, it is imperative to examine the validity of the 'equivalent' problem used to solve the latter. Two numerical simulations were performed, with conical tips ($\alpha = 70.3^{o}$) indenting on notched specimens (to emulate plastic imprints), such that α' equals to 85^{o} and 89^{o}, respectively. From Fig. 3, the values of α' chosen correspond to E/σ_y of approximately 25 and 500 respectively, which are representative for a wide range of common materials. Figure 7(a) illustrates the indenter and specimen before reloading, while Fig. 7(b) shows them at maximum depth, h_{max}.

Figure 8 shows the load-displacement curves for the indentation of notched specimens with α' equals 85^{o} and 89^{o} obtained from the numerical simulations, and their comparison with Sneddon's solution (1), plotted with the corresponding α'. The simulation results were found to coincide with their analytical counterpart for both values of α'. These results agree with the works of other researchers (Sakai, 2003; Stilwell and Tabor, 1961) – provided (1) the residual impression has flat sides even after elastic recovery and (2) the reloading of impression is elastic and reversible, then the load-displacement reloading path is quadratic and may be characterized by a single geometrical parameter, in this case α'. This suggests that the equivalent problem that involved solely geometrical differences is indeed valid; however, the actual unloading of a plastic imprint involves the effects of residual stresses as well. Thus, it is unlikely that this sole geometrical parameter, α' is sufficient to describe the equivalent indenter. This point will be discussed in more details in the subsequent section.

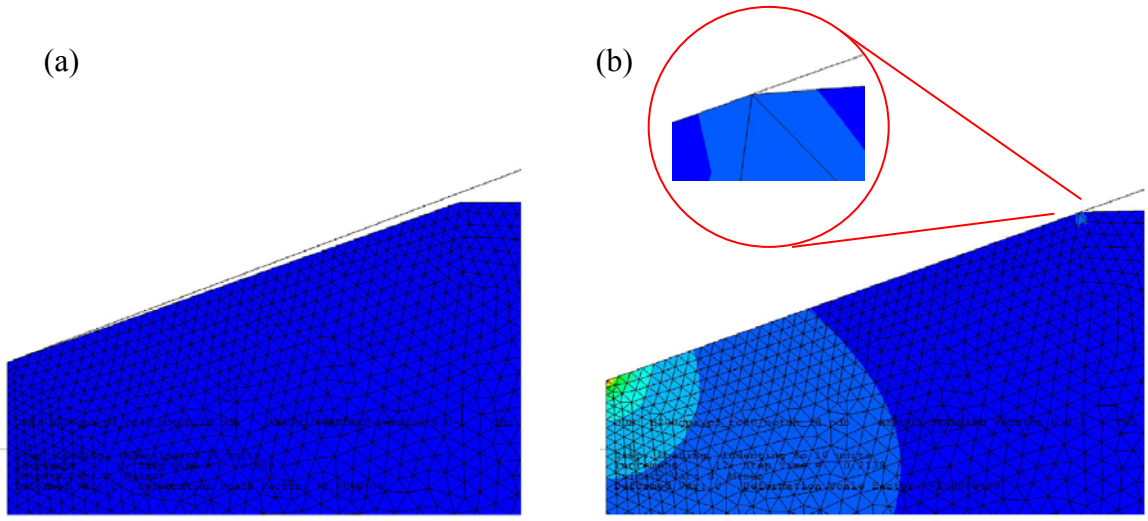

Fig. 7. (a) Indentation of a notched specimen, (b) At h_{max}, the radius of contact is equal to the radius of the residual imprint.

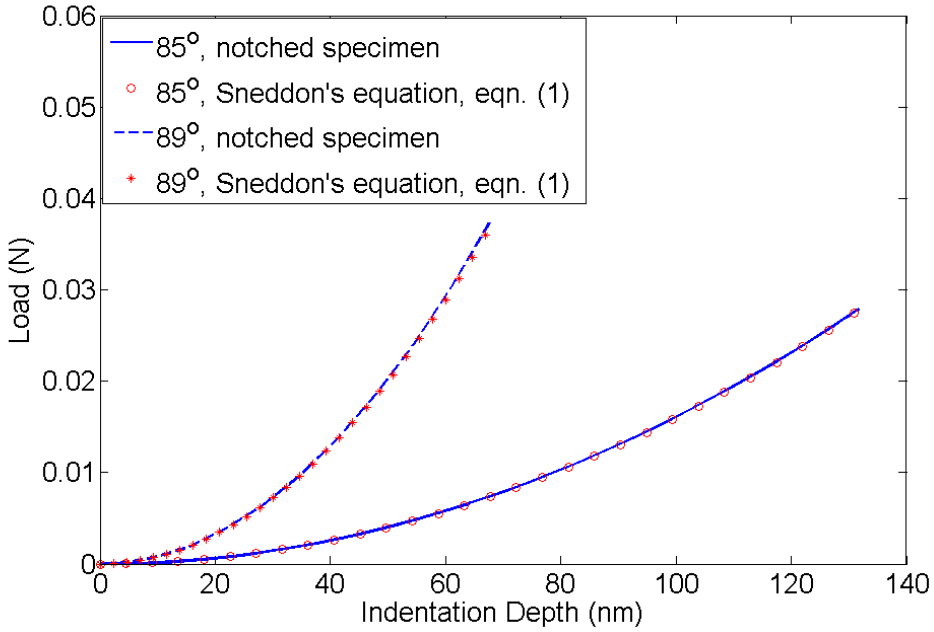

Fig. 8. Load-displacement curves for $\alpha' = 85^{o}$ and 89^{o}.

3.4 The straightforward application of Sneddon's equation

Having validated the elastic unloading and equivalent problem assumption, it may seem logical to use Sneddon's elastic relation (1) directly, with an appropriate α', to take into account the plastic imprint. This will eliminate the uncertainty introduced in the measurement of the

slope of the unloading load-displacement curve, dP/dh_e, which is a required parameter for the conventional derivation of the elastic modulus, as shown in (6).

The unloading curve from an elastic-plastic indentation was compared with the elastic load-displacement relationship obtained using (1), to examine the accuracy of the straightforward application of Sneddon's equation. Figure 9 shows the comparison between the simulated unloading curve and the elastic reloading curves with calculated and 'ideal' $\alpha's$. The calculated α' refers to the effective angle derived using (4), which is found to be 88.1°. The ideal α' refers to the effective angle that will give the correct E when substituted into (1), which is found to be 88.9°.

The two elastic curves obtained using (1) are observed to be distinctly different from the actual unloading curve. The curve plotted with the ideal α', only meets the unloading curve at h_{max}. This suggests that the reason behind the mismatch of the curves is not due to the wrong choice of α'.

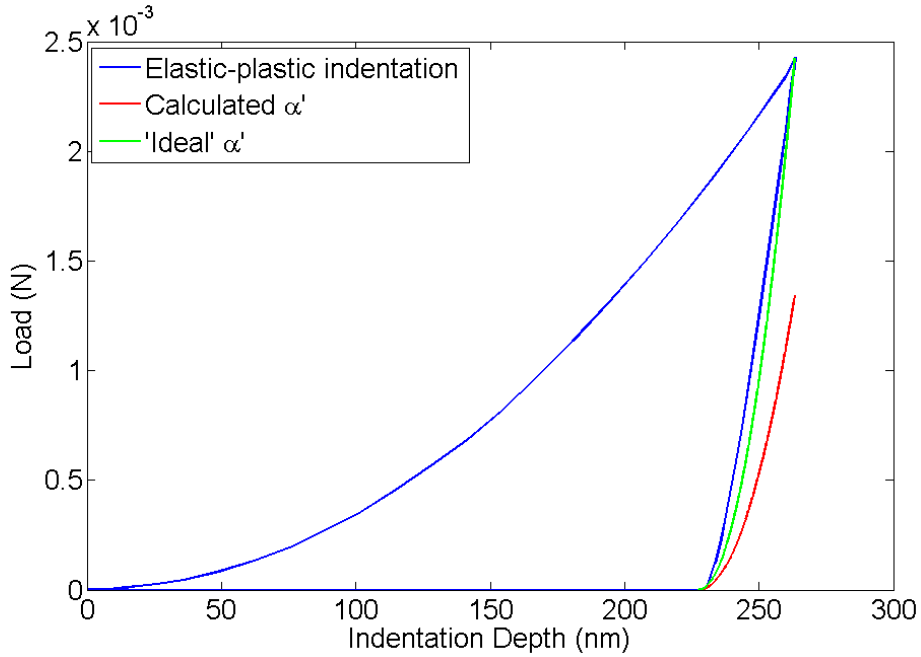

Fig. 9. Comparison between the simulated unloading curve and the elastic reloading curves with calculated and 'ideal' α's.

One reason for this discrepancy is the curvature of the walls of the imprint. Figure 10 shows profiles of the residual imprint for E/σ_y of 10 and 1000 respectively. From Fig. 10(a), it is observed that the walls of the residual imprint are not flat as assumed in the 'equivalent' problem. Thus, the actual problem cannot be simply described by the indentation of a notched specimen with half-angle $\alpha+\alpha^*$, as illustrated in Fig. 2. According to Pharr *et al.* (2002) , the effective indenter shape in this case is no longer conical, but instead is a parabola of revolution. This is because the actual problem is now an indentation of a curved surface with a conical indenter, and following the same reasoning as the proposition of the equivalent problem before, it is expected that the equivalent problem is now an indentation of an indenter with a curved profile on a flat surface.

Hence, for elastic-plastic indentations using conical indenters, the straightforward application of Sneddon's elastic relation (1948) as shown in (1) to the unloading curve, is not appropriate.

The conventionally used relation, shown by (6), is applicable to indenters that are bodies of revolution, and have a profile that is C^{∞}, i.e., infinitely smooth (Pharr, *et al.*, 1992). Thus, it is suitable for the effective indenter shape, which was established to be a parabola of revolution. The factors affecting the accuracy of (6) are examined next.

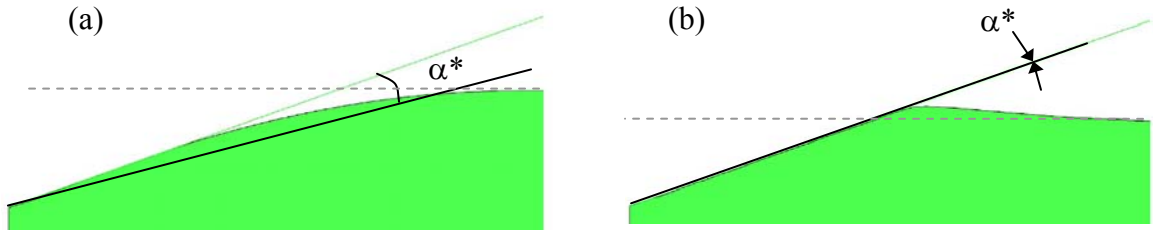

Fig. 10. (a) Profile of the residual imprint for E/σ_y=10, (b) Profile of the residual imprint for E/σ_y=1000. (Note the sink-ins and pile-ups).

3.5 Factors affecting the accuracy of the conventional relation

3.5.1 Residual stresses at the plastic imprint

Residual stresses are present at the plastic imprint during the unloading process of the elastic plastic indentation and they cannot be neglected. Pharr and Bolshakov (2002) introduced the concept of the effective indenter to account for the surface distortion and pressure distribution under the indenter, however, the interaction between the residual stresses and the surface geometry of the plastic imprint and their combined effects on the shape of the effective indenter through the exponent of the unloading load-displacement relationship is not clear.

The Poisson's ratio, ν of the specimen is an important parameter that dictates the level of residual stresses present at the plastic imprint, as can be observed in Fig. 11. This figure shows that as ν tends towards 0.5, the extent of residual equivalent stress present at the plastic imprint decreases significantly. This can be qualitatively understood in terms of the elastic constraint exerted on the plastic zone. This observation may also possibly explain why the percentage error

for the extracted E using the conventional method is so much dependent on v, and why it decreases as v approaches 0.5, as observed in Fig. 5.

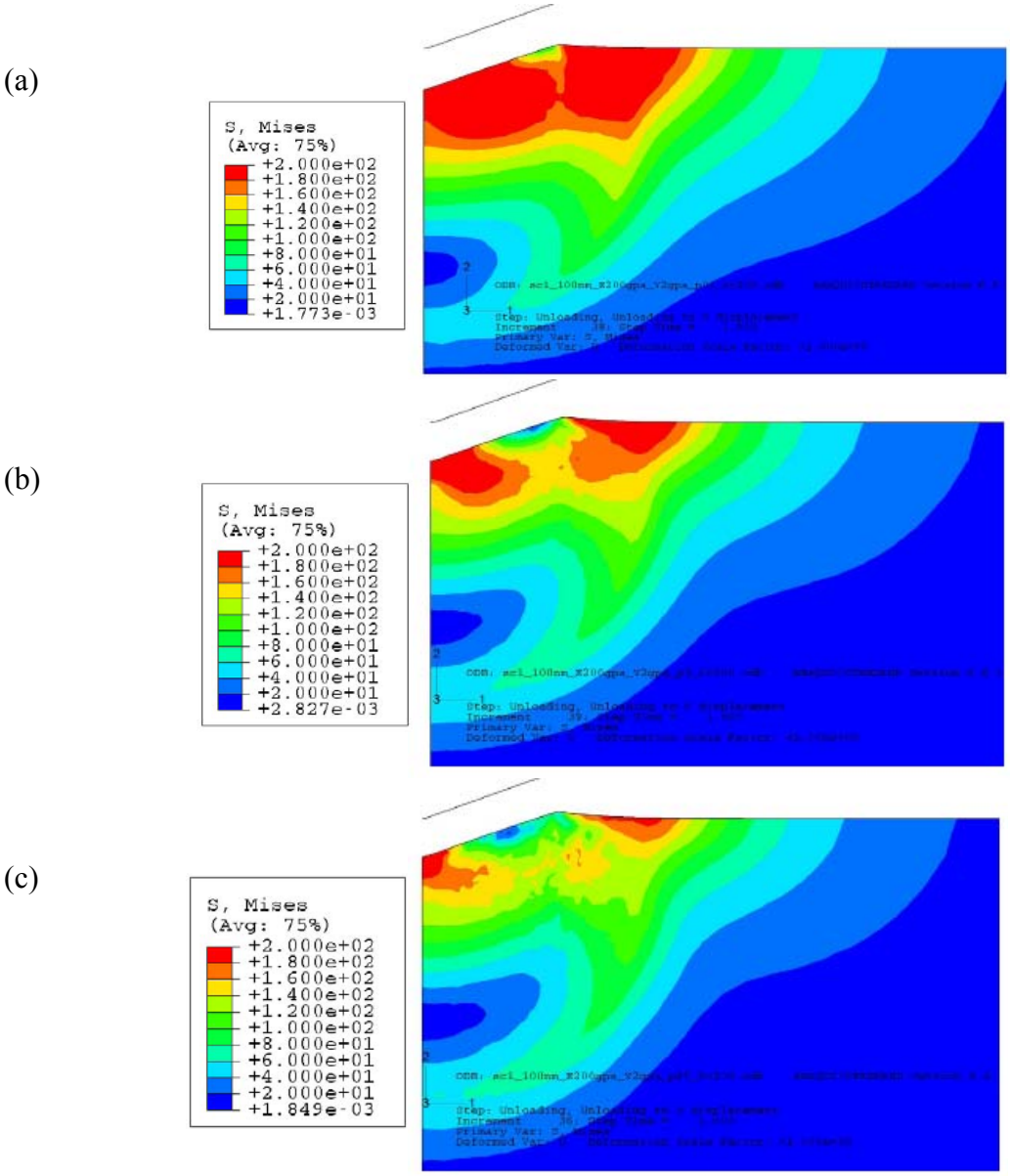

Fig. 11. Residual equivalent (Mises) stress fields for indentations of elastic, perfectly plastic material with $E = 200$ GPa, $\sigma_y = 2$ GPa, and different υ (= 0.01, 0.3 and 0.45, respectively). (Note that the stress values must be multiplied by a factor of 1e7 to respect the scale of the problem).

3.5.2 Accurate determination of A.

3.5.2.1 The contact depth, h_c

The projected contact area, A is a function of the contact depth, h_c, through the known or measured geometry of the indenter. Thus, the accurate determination of h_c is crucial for the extraction of elastic constants using (6).

It is observed from Fig. 10(b) that when E/σ_y is large and the hardening coefficient n is small, there are pile-ups around the plastic imprint. This will result in the actual contact depth, h_c, to deviate significantly from that derived by (8). This deviation has been studied extensively and found to be more than 30% in some cases (Cheng and Cheng, 2004). While some researchers may argue that pile-ups are only significant when $h_r/h_{max} > 0.7$ (Oliver and Pharr, 2004), this criterion corresponds to $E/\sigma_y > 30$, for elastic-perfectly plastic materials, using (10), and is also evidenced by the numerical simulations of Pharr and Bolshakov (2002). This stringent criterion severely limits the applicability of (8) to accurately determine h_c for typical materials.

3.5.2.1 Finite tip radius of the indenter

It has been established that in the case of a linearly elastic indentation, finite tip radius effects are significant (Poon, *et al.*, 2008). Unlike the elastic case, the loading and unloading segments for the elastic-plastic indentation do not coincide. Thus, the effects of the finite tip radius of the indenter, ρ, will be discussed separately for the loading and unloading stages of the elastic-plastic indentation.

The loading curve of the elastic-plastic indentation is expected to be sensitive to finite tip radius effects. Similar to the arguments for the indentation of linearly elastic solids, a blunt indenter is expected to require a larger force to penetrate to a fixed arbitrary depth. In addition, ρ will affect the projected contact area, A at the maximum indentation depth. These effects have been extensively studied by researchers (Cheng and Cheng, 1998; Troyon and Huang, 2004).

On the other hand, the unloading curve of the elastic-plastic indentation is expected to be insensitive to finite tip radius effects. This is evidenced by two observations. First, it is observed that for a typical range of E/σ_y between 100 and 1000, the effective half-angle, α' is between 88° and 89.7°. As α' tends to 90°, the effect of ρ is expected to become less dominant. This phenomenon can be interpreted from the location of the transition point, h_a, given by,

$$h_a = \rho(1 - \sin\alpha') , \tag{12}$$

where h_a is defined as the depth which the spherical tip (with radius = ρ) is tangential to the sides of the cone with half-angle, α'. As α' tends towards 90°, h_a becomes vanishingly small, regardless of the tip radius. This suggests that the finite tip radius of the indenter does not play a dominant role in the elastic unloading/reloading process of the indentation.

For situations where the walls of the plastic imprint may not be described by a single geometrical parameter, α', the effect of ρ can be explained with the pressure distribution under the indenter. Pharr and Bolshakov (2002) demonstrated that the pressure distribution under the indenter at peak load is relatively constant and suggested that the equivalent problem amounts to the indentation of an elastic flat half-space with an effective parabolic indenter. The effective parabolic indenter takes no account of the local ρ, which suggests that the finite tip radius effects are unlikely to affect the elastic unloading curve significantly.

However, one should keep in mind that unloading follows active loading for which the finite tip radius does indeed affect the projected area of contact, A. The latter, in turn, determines the accuracy of the conventional method for the extraction of elastic properties of the material. These results are tabulated in Tables 1 and 3 in the Appendix.

4. PROPOSED TECHNIQUE

Load and displacement measurements are recorded in nanoindentation experiments, so that the slope of the unloading segment can be calculated using (6), leaving the projected contact area, A as the only unknown in the equation. Therefore, the primary challenge to reduce the errors involved in the derivation of the reduced modulus E_r, lies in the accurate measurements of the projected contact area, A.

As discussed in the previous section, the accurate determination of A is dependent on the accurate derivation of h_c and ρ. Pile-ups, as shown in Fig. 12, underestimate h_c and thus underestimate the actual projected contact area, A. For elastic-plastic materials that strain-harden, it has been shown that the extent of hardening reduces the amount of pile-ups, and it is even possible for the material to sink-in (Cheng and Cheng, 1999), i.e., (8) overestimates the actual projected contact area, A.

The neglect of finite tip radius effects will result in the underestimation of A as well. Suppose a conical indenter with a finite tip radius may be represented by a cone with a spherical cap, the projected contact area, A is given by (Troyon and Huang, 2004),

$$A = \pi \tan^2 \alpha (h_c + h_b)^2 , \tag{13}$$

where h_b is the blunting distance, which is the distance between the supposed apex of the cone and the spherical cap. Since h_b is a positive variable that represents the finite tip radius effects, if neglected will result in an underestimation of the projected contact area, A.

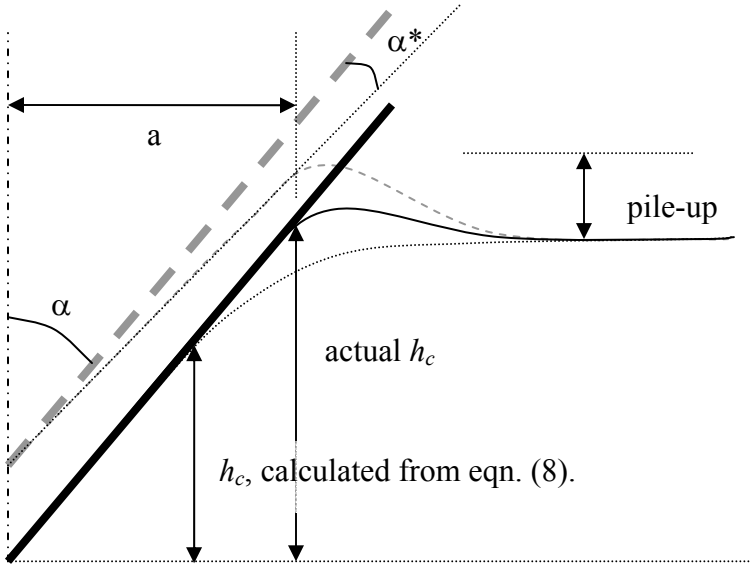

Fig. 12. Schematic of an elastic-plastic indentation

Although it is clear that the accurate determination of the projected contact area, A is central to the accurate extraction of E_r, such a determination is currently missing. The accurate determination of the tip radius of the indenter, ρ is not a trivial task, yet, even with an accurate knowledge of ρ, one still requires the knowledge of h_c to accurately determine A. It is established that h_c is affected by pile-ups and sink-ins that are themselves determined by the material constitutive behavior, which is precisely what one seeks to characterize using nanoindentations. Proposed methods to approximate h_c, are often valid for certain range of material properties, which might result in a severe overestimation or underestimation of the material property values (Tranchida, *et al.*, 2006). Thus, the subsequent section proposes an experimental technique to measure the projected contact area, *A directly* without any assumptions or restrictions on material properties.

4.1. Measurement of the projected contact area in indentation/nanoindentation tests using electrical resistance method

A simple methodology is proposed for the in-situ measurement of the contact area, A. It is based on the following 2 steps:

a. determine r, the specific electrical contact resistance between the tip and the substrate. For this, bring a cylindrical (or equivalently well defined) conductive tip of known cross-sectional area to be in contact with the sample.

b. using a conventional tip (such as Berkovich) with the same material as the tip used in the calibration, the measured current is directly related to the surface area of contact, A_s using the relation $I = A_s r$. The projected area of contact, A can then be inferred from A_s, based on the known geometry of the indenter.

The proposed method is simple and straightforward. The measured projected area takes into account any pile-ups or sink-ins associated with the properties of the sample.

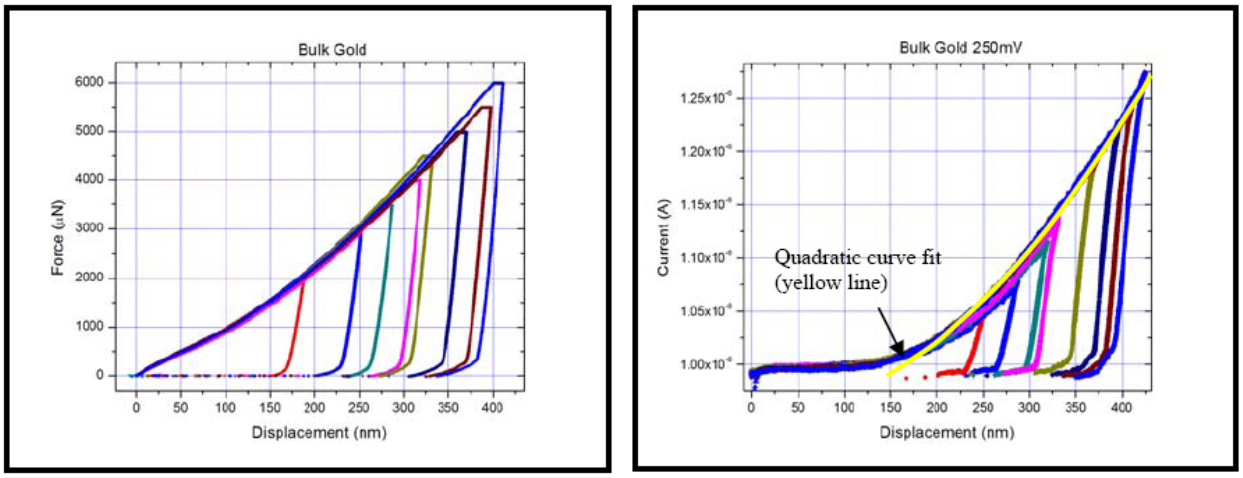

Fig. 13. (a) Load-displacement curves for the indentations of polycrystalline Gold (Au); (b) Corresponding current-displacement curves for the indentations (courtesy of Hysitron (Vodnick, 2007)).

Figure 13(a) shows the load-displacement curves for the indentations of polycrystalline gold, using a Berkovich tip, and Fig. 13(b) shows the corresponding in situ measurement of the current-displacement curves. Figure 13(b) was discretized and fitted with a quadratic curve with no linear term. The current-displacement relation is well described by the fitted quadratic curve,

as expected (R^2 = 0.994). The current is expected to increase with surface contact area, which varies with the square of indentation depth. Thus, the current measured across the tip/specimen contact should vary proportionally with the square of the indentation depth. It is also observed that at shallow indentation depths, the current does not fit as well to the quadratic curve. This is probably due to the finite tip radius of the indenter. Nonetheless, this preliminary analysis shows that the proposed methodology for the measurement of projected contact area, A, is very promising. However, it is important to note that the accuracy of this technique can be affected by changes in the material properties during indentation, such as phase changing or formation of shear bands, or presence of surface asperities affecting the accurate measurement of the surface area of contact as discussed by researchers such as Mann *et al.* (2002) and Ruffell *et al.* (2007).

4.2. Reduction of errors with accurate measurement of A

To investigate the reduction of errors from the accurate measurement of A, the Young's modulus, E (with *a priori* knowledge of v) was calculated using (6) with accurate measurements of A from the numerical simulations. The results are tabulated in Tables 6 and 7 in the Appendix.

Figure 14 plots the percentage error, ε vs. E/σ_y for the range of v (0.01, 0.3 and 0.47) and ρ (30 *nm* and 150 *nm*), using A, calculated from (7), and measured directly in the simulations. It is observed that for the range of E/σ_y relevant to most materials, i.e., between 100 and 1000, ε is reduced by more than 50%. It is also observed that when E/σ_y is small, the difference between A calculated using (7) and that measured in the simulation is not significant. When E/σ_y is small (say, <30), the extent of plasticity is not prevalent, the $h_r/h_{max} < 0.7$ criterion for the accurate use of (8) is fulfilled. Hence, the measured value of A is expected to be similar to that derived using elastic relations. In addition, when the accurate value of A is used, ε is observed to be relatively insensitive to E/σ_y.

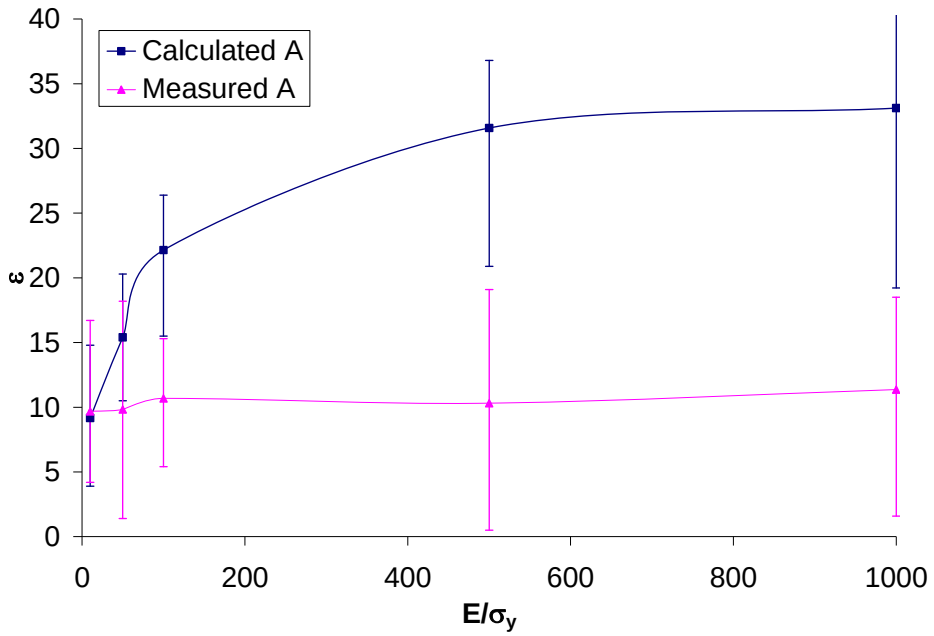

Fig. 14. ε vs. E/σ_y, using calculated and "measured" values for A. The bars correspond to the calculated range of ε for values of ν (= 0.01, 0.3, 0.47) and ρ (= 30 *nm*, 150 *nm*). Exact values are tabulated in Tables 1, 3, 6 and 7.

The percentage error of the extracted E, ε is also found to be insensitive to the tip radius of the indenter when the accurate projected area, A was used in the extraction of E, as can be observed from Fig. 15. This result confirms the previous hypothesis that the finite tip radius of the indenter only affects the accurate determination of A.

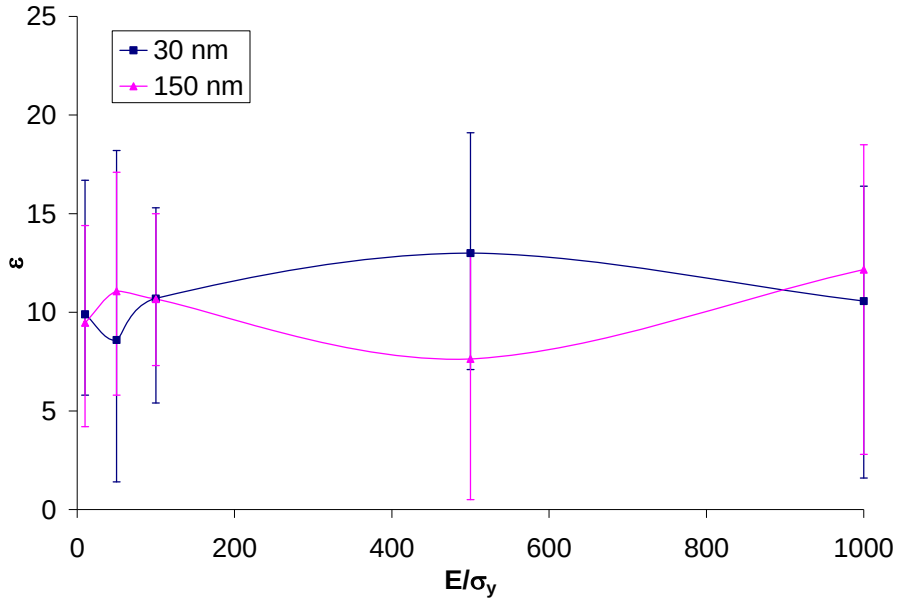

Fig. 15. ε vs. E/σ_y, using "measured" values for A for ρ = 30 *nm* and 150 *nm*. The bars correspond to the range of ε for values of υ (=0.01, 0.3, 0.47). Exact values are tabulated in Tables 6 and 7.

From Fig. 16, it is observed that the percentage error of the extracted E, using the measured A, is sensitive to v. This suggests that this error associated with v is independent of the accurate determination of A. Though it has been shown that the extent of residual stress at the plastic imprint is sensitive to v of the indented material, it is not clear how the residual stresses affect the accuracy of the extracted elastic properties of interest.

For linearly elastic indentations, it was established that the correction factor, β is the product of the first correction factor term, $f(v)$ due to radial displacement (Hay, *et al.*, 1999) and a form factor essentially related to the geometry of contact (Poon, *et al.*, 2008). For elastic-plastic indentations, the present discussion assumed that the projected contact area, A is accurately determined. Hence, in the context of β in the linearly elastic case, the form factor is effectively unity. Furthermore, ε for the elastic-plastic indentations is observed to be relative insensitive to E/σ_y and ρ, such that ε may be interpreted as a function of only v. Figure 17 compares the correction factor, $f(v)$ associated with v in elastic and elastic-plastic indentations. It is observed

that $f(v)$ for both cases are rather similar although $f(v)_{\text{elastic-plastic}}$ is observed to be consistently larger than $f(v)_{\text{elastic}}$. It is important to note that $f(v)_{\text{elastic}}$ is attributed to the negligence of radial displacement in Sneddon's derivation whereas $f(v)_{\text{elastic-plastic}}$ is likely associated with the residual stress field around the plastic imprint due to elastic confinement. Figure 17 shows why even though the correction factor, $f(v)$ is fundamentally different for both linearly elastic and elastic-plastic case, the use of $f(v)_{\text{elastic}}$ for elastic-plastic indentations do not result in significant errors.

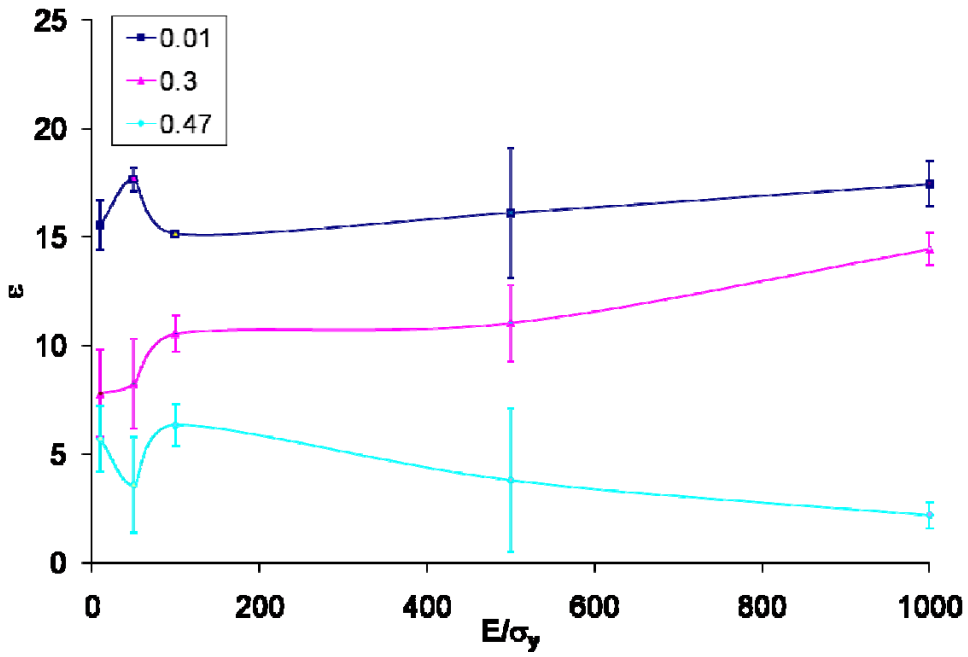

Fig. 16. ε vs. E/σ_y, using "measured" values for A for υ =0.01, 0.3 and 0.47. The bars correspond to the range of ε for values of ρ (= 30 *nm* and 150 *nm*). Exact values are tabulated in Tables 6 and 7.

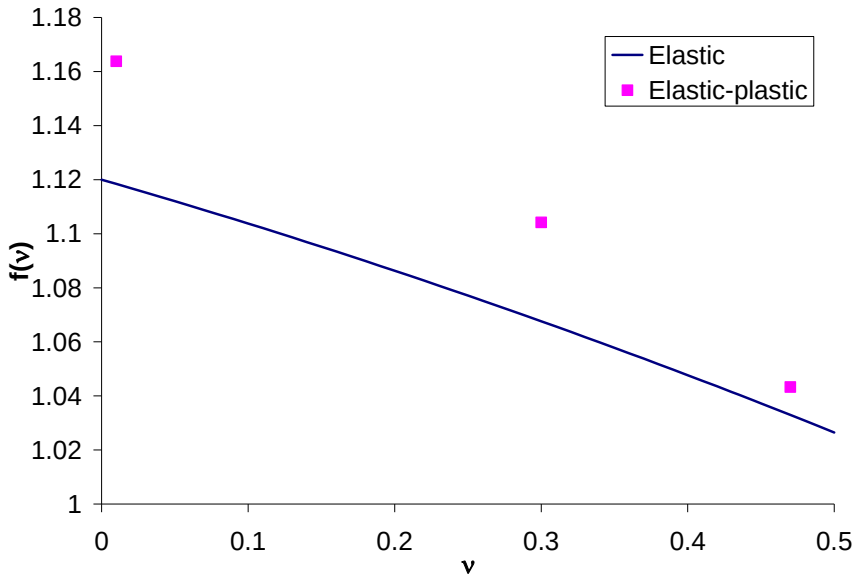

Fig. 17. Comparison between the correction factor, $f(\nu)$ between elastic and elastic-plastic indentations.

It is important to note that there are still secondary sources of error in the derivation of elastic constants. One important source of error lies in the measurement of the slope of the unloading curve. Despite measures taken to reduce them such as curve fitting, an uncertainty of up to 5% can be introduced to the measurement of the slope. This uncertainty will then be propagated to the value of E_r.

5. SUMMARY AND CONCLUSIONS

The conventional method of deriving elastic constants using nanoindentation of elastic-plastic materials has been critically examined using numerical simulations and experiments. The main results of this study are summarized below:

The effective half-angle, α' has been identified to be a function of E/σ_y, as shown in Fig. 3. For a typical material, E/σ_y ranges between 100 and 1000, thus its corresponding α' ranges between 88^o and 89.7^o. However, this single geometrical parameter α' cannot adequately

represent the residual stress field, which is a function of Poisson's ratio of the specimen, v that characterizes the unloading stage of the elastic-plastic imprint. Consequently, Sneddon's load-displacement relationship for the conical indenter (1) cannot effectively describe the elastic unloading curve of an elastic-plastic indentation. Therefore, it seems preferable to use the elastic relationship for axially symmetric indenters with a smooth profile (6). Yet, (6) requires an accurate determination of the projected area of contact, A. The latter may be inferred analytically provided $h_r/h_{max} < 0.7$, but for an elastic-perfectly plastic material, this criterion is equivalent to $E/\sigma_y < 30$, which is quite limited in scope for most materials of interest. Pile-ups and sink-ins will also affect the accuracy of h_c , and thus A, but they are in turn determined by the very mechanical properties of the investigated material, which are to be determined. In addition, A is also found to be a function of the indenter's tip-radius, ρ, through the elastic-plastic loading stage of the indentation cycle. Therefore, an alternative approach is proposed, in which A is measured directly, using electrical methods. The viability of this method has been verified based on experimental results. Once A is accurately determined, one observes that the percentage error of the extracted Young's modulus is insensitive to E/σ_y and ρ as expected, but it is still sensitive to v.

Concerning the determination of the yield strength of the material, a power law relationship was identified between h_e/h_{max} and E/σ_y in (9). This relation was verified experimentally and found to provide an upper bound for the yield stress of pressure sensitive and/or strain hardening materials.

In conclusion,

- The direct application of Sneddon's solution for elastic-plastic indentations is not as appropriate as the conventional method (6).

- The residual stress field around the plastic imprint is found to be sensitive to the Poisson's ratio, v. Higher values of v correspond to lower residual stresses.
- An accurate determination of the projected contact area, A will reduce the errors in the extracted value of E by more than 50% for typical elastic-plastic solids.
- The projected contact area, A is found to be not only related to h_c but also to E/σ_y and ρ as well.
- A new experimental procedure to directly measure the projected contact area, A is proposed.
- A new methodology to extract the yield stress of materials using nanoindentation has been proposed.

ACKNOWLEDGMENTS

The research reported here was supported by the National Science Foundation (DMR # 0520565) through the Center for Science and Engineering of Materials (CSEM) at the California Institute of Technology is acknowledged. GR gratefully acknowledges the Ronald and Maxine Linde Venture Fund that enabled the acquisition of the Hysitron^{TM} Triboindenter used in this investigation. DR acknowledges the support of his visit to Caltech made possible through the Clark Millikan Visiting Professorship in Aeronautics. We would like to acknowledge A. Fischer-Cripps for useful discussions and communications and D. Vodnick for providing the data in Fig. 13.

REFERENCES

Atkins, A.G., Tabor, D., 1966. Hardness and deformation properties of solids at very high temperatures. Proc. Roy. Soc. A292, 441-459.

Bower, A.F., Fleck, N.A., Neddleman, A., Ogbonna, N., 1993. Indentation of a power-law creeping solid. Proc. R. Soc. A441, 97-124.

Bulychev, S.I., Alekhin, V.P., Shorshorov, M.K., Ternovskii, A.P., Shnyrev, G.D., 1975. Determining Young's Modulus from the Indentor Penetration Diagram. Zavodskaya Laboratoriya 41 (9), 1137-1140.

Cheng, Y.T., Cheng, C.M., 1998. Further analysis of indentation loading curves: Effects of tip rounding on mechanical property measurements. J. Mater. Res. 13 (4), 1059-1064.

Cheng, Y.T., Cheng, C.M., 1999. Scaling Relationships in Conical Indentation of Elastic Perfectly Plastic Solids. Int. J. Solids Structures 36, 1231-1243.

Cheng, Y.T., Cheng, C.M., 2004. Scaling, dimensional analysis, and indentation measurements. Mat. Sci. and Engng. R 44, 91-149.

Fischer-Cripps, A.C., 2004. Nanoindentation. Springer.

Hansen, N., Huang, X., 1998. Microstructure and Flow stress of Polycrystals and Single Crystals. Acta Materialia 46 (5), 1827-1836.

Hay, J.C., Bolshakov, A., Pharr, G.M., 1999. A Critical Examination of the Fundamental Relations Used in the Analysis of Nanoindentation Data. J. Mater. Res. 14, 2296-2305.

Hill, R., Lee, E.H., Tupper, S., 1947. The Theory of Wedge Indentation of Ductile Materials. Proc. R. Soc. Lond. A 188 (1013), 273-289.

Kutty, T.R.G., Ganguly, C., Sastry, D.H., 1996. Development of creep curves from hot indentation hardness data Scripta Materialia 34 (12), 1833-1838.

Lawn, B.R., Evans, A.G., Marshall, D.B., 1980. Elastic/plastic indentation damage in ceramics: The median/radial crack system. J. American Ceramic Soc. 63 (9-10), 574-581.

Loubet, J.L., Georges, J.M., Marchesini, O., Meille, G., 1984. Vickers Indentation Curves of Magnesium Oxide {MgO}. J. Tribol-T ASME 106, 43-48.

Mann, A.B., Heerden, D.V., Pethica, J.B., Bowes, P., Weihs, T.P., 2002. Contact resistance and phase transformations during nanoindentation of silicon. Philos. Mag. A 83 (10), 1921-1929.

Martin, M., Troyon, M., 2002. Fundamental relations used in nanoindentation: Critical examination based on experimental measurements. J. Mater. Res. 17 (9), 2227-2234.

Mayo, M.J., Nix, W.D., 1988. A microindentation study of superplasticity in Pb, Sn, and Sn-38wt%Pb. Acta Metall. 36 (8), 2183-2192.

Miyake, K., Fujisawa, S., Korenaga, A., Ishida, T., Sasaki, S., 2004. The Effect of Pile-up and Contact Area on Hardness test by Nanoindentation. Jap. J. of Appl. Phys. 43 (7B), 4602-4605.

Newey, D., Wilkins, M.A., Pollock, H.M., 1982. An Ultra-Low-Load Penetration Hardness Tester. J. Phys. E: Sci. Instrum. 15, 119-122.

Oliver, W.C., Pharr, G.M., 2004. Review: Measurement of Hardness and Elastic Modulous by Instrumented Indentation: Advances in Understanding and Refinements to Methodology. J. Mater. Res. 19, 3-20.

Palmqvist, S., 1957. A method to determine the toughness of brittle materials, especially hard materials. Jernkontorets Ann. 141, 303-307.

Payzant, E.A., King, H.W., Gupta, S.D., Jacobs, J.K., 1993. Hot hardness of ceramic cutting tools using depth of penetration measurements. In: Mostaghaci, H., Drew, R.A.L. (Eds.), Development and Applications of Ceramics and New Metal Alloys. Canadian Institute of Mining and Metallurgy, Montreal, pp. 399-408.

Pethica, J.B., Hutchings, R., Oliver, W.C., 1983. Hardness Measurement at Penetration Depths as Small as 20 Nm. Philos. Mag. A 48, 593-606.

Pharr, G.M., Bolshakov, A., 2002. Understanding Nanoindentation Unloading Curves. J. Mater. Res. 17, 2660-2671.

Pharr, G.M., Oliver, W.C., Brotzen, F.R., 1992. On the Generality of the Relationship Among Contact Stiffness, Contact Area, and the Elastic Modulus During Indentation. J. Mater. Res. 7 (3), 613-617.

Poon, B., Rittel, D., Ravichandran, G., 2008. An Analysis of Nanoindentation in Linearly Elastic Solids. Submitted to the Int. J. Solids Structures.

Ruffell, S., Bradby, J.E., Williams, J.S., Warren, O.L., 2007. An in situ electrical measurement technique via a conducting diamond tip for nanoindentation in silicon. J. Mater. Res. 22 (3), 578-586.

Sakai, M., 2003. Elastic recovery in the unloading process of pyramidal microindentation. J. Mater. Res. 18 (7), 1631-1640.

Shiwa, M., Weppelmann, E.R., Munz, D., Swain, M.V., Kishi, T., 1996. Acoustic emission and precision force-displacement observations on pointed and spherical indentation of silicon and TiN film on silicon. J. Mater. Sci. 31, 5985-5991.

Sneddon, I.N., 1948. Boussinesq's Problem for a Rigid Cone. Proc. Cambridge Philos. Soc., 492-507.

Stilwell, N.A., Tabor, D., 1961. Elastic recovery of conical indentations. Proceedings of the Physical Society of London 78 (500), 169.

Storåkers, B., Larsson, P.L., 1994. On Brinell and Boussinesq Indentation of Creeping Solids. J. Mech. Phys. Solids 42, 307-332.

Tabor, D., 1948. A Simple Theory of Static and Dynamic Hardness. Proc. R. Soc. Lond. A 192 (1029), 247-274.

Tabor, D., 1951. The Hardness of Metals. Oxforf University Press, Cambridge, Great Britain.

Ternovskii, A.P., Alekhin, V.P., Shorshorov, M.K., Khrushchov, M.M., Skvortsov, V.N., 1974. Micromechanical Testing of Materials by Depression. Zavodskaya Laboratoriya 39 (10), 1242-1247.

Tranchida, D., Piccarolo, S., Loos, J., Alexeev, A., 2006. Accurately evaluating Young's modulus of polymers through nanoindentations: A phenomenological correction factor to Oliver and Pharr procedure. Appl. Phys. Lett 89, 171905-171901-171903.

Troyon, M., Huang, L., 2004. Correction factor for contact area in nanoindentation measurements. J. Mater. Res. 30 (3), 610-617.

Tymiak, N.I., Daugela, A., Wyrobek, T.J., Warren, O.L., 2003. Highly localized acousticemission monitoring of nanoscale indentation contacts. J. Mater. Res. 18 (4), 784-796.

Vodnick, D.J., 2007. Force vs. Displacement and Current vs. Displacement plots for polycrystalline Gold. Personal communication. In: Poon, B. (Ed.).

APPENDIX

E/σ_y	*he* (nm)	α'	Calculated E (GPa)	% Error
E = 50GPa, ν = 0.01, ρ = 30nm				
10	135.3	80.7°	55.6	11.3
50	55.53	86.9°	58.1	16.3
100	34.15	88.2°	61.8	23.7
500	10.48	89.5°	68.4	36.8
1000	7.03	89.7°	69.6	39.3
E = 50GPa, ν = 0.3, ρ = 30nm				
10	161.68	78.6°	53.4	6.8
50	56.48	86.8°	56.7	13.3
100	35.95	88.1°	61.3	22.5
500	11.95	89.4°	64.5	29.0
1000	7.41	89.6°	64.7	29.4
E = 50GPa, ν = 0.47, ρ = 30nm				
10	161.68	78.5°	51.9	3.9
50	61.57	86.5°	55.2	10.5
100	32.95	88.2°	60.8	21.6
500	9.57	89.5°	64.9	30.0
1000	6.47	89.4°	59.6	19.2

Table 1: Varying Poisson's Ratio, ν, with E = 50GPa and ρ = 30nm

E/σ_y	*he* (nm)	*A′*	Calculated *E* (GPa)	% Error
E = 10GPa, ν = 0.3, ρ = 30nm				
10	161.68	78.6°	10.7	6.61
50	56.47	86.8°	11.5	14.7
100	35.95	88.1°	12.4	24.3
500	11.95	89.4°	13.2	32
1000	7.41	89.6°	13.1	31
E = 50GPa, ν = 0.3, ρ = 30nm				
10	161.68	78.6°	53.4	6.8
50	56.48	86.8°	56.7	13.3
100	35.95	88.1°	61.3	22.5
500	11.95	89.4°	64.5	29.0
1000	7.41	89.6°	64.7	29.4
E = 100GPa, ν = 0.3, ρ = 30nm				
10	161.68	78.6°	106.1	6.1
50	56.47	86.8°	113.3	13.3
100	35.95	88.1°	123.6	23.6
500	11.95	89.4°	129.9	29.9
1000	7.41	89.6°	131.4	31.4

Table 2: Varying Young's modulus, *E*, with ν = 0.3 and ρ = 30nm

E/σ_y	*he* (nm)	α'	Calculated *E* (GPa)	% Error
E = 50GPa, ν = 0.01, ρ = 150nm				
10	138.64	80.4°	57.4	14.8
50	53.26	87.0°	60.1	20.3
100	34.50	88.2°	63.2	26.4
500	10.48	89.5°	68.4	36.8
1000	6.02	89.7°	74.8	49.6
E = 50GPa, ν = 0.3, ρ = 150nm				
10	161.68	78.4°	55.3	10.5
50	58.82	86.7°	58.6	17.3
100	36.33	88.1°	61.6	23.2
500	11.50	89.4°	68.0	36.0
1000	6.36	89.7°	69.4	38.9
E = 50GPa, ν = 0.47, ρ = 150nm				
10	161.68	78.4°	53.8	7.7
50	58.79	86.7°	57.3	14.7
100	37.22	88.0°	57.8	15.5
500	13.05	89.3°	60.5	20.9
1000	10.14	89.5°	61.2	22.3

Table 3: Varying Poisson's Ratio, υ, with E = 50GPa and ρ = 150nm

E/σ_y	*he* (nm)	*A′*	Calculated *E* (GPa)	% Error
E = 10GPa, ν = 0.3, ρ = 150nm				
10	161.68	78.4°	11.0	10.4
50	58.82	86.7°	11.7	16.6
100	36.33	88.1°	12.4	24.1
500	11.50	89.4°	13.8	38.0
1000	6.36	89.7°	14.5	44.9
E = 50GPa, ν = 0.3, ρ = 150nm				
10	161.68	78.4°	55.3	10.5
50	58.82	86.7°	58.6	17.3
100	36.33	88.1°	61.6	23.2
500	11.50	89.4°	68.0	36.0
1000	6.36	89.7°	69.4	38.9
E = 100GPa, ν = 0.3, ρ = 150nm				
10	161.68	78.4°	110.4	10.4
50	58.82	86.7°	117.3	17.3
100	36.33	88.1°	125.3	25.3
500	11.50	89.4°	138.0	38.0
1000	6.36	89.7°	139.9	39.9

Table 4: Varying Young's modulus, E, with ν = 0.3 and ρ = 150nm

Specimen	Number of experiments	E/σ_y (from known values)	Mean (h_e/h_{max} from experiments)	Standard Deviation (h_e/h_{max} from experiments)
Aluminum	12	1750	0.0181	0.0055
Fused Quartz	6	68.2	0.5609	0.0171
Pt BMG	12	67.7	0.2516	0.0356
Homalite	14	79.9	0.5900	0.0938
Silicon	3	145.5	0.6305	0.0087

Table 5: Statistical variation for nanoindentation experiments.

E/σ_y	Calculated A (μm^2)	"Measured" A (μm^2)	Calculated E (with "measured" A) (GPa)	% Error
E = 50GPa, ν = 0.01, ρ = 30nm				
10	0.87	0.79	58.4	16.7
50	1.33	1.28	59.1	18.2
100	1.47	1.69	57.7	15.3
500	1.64	2.17	59.5	19.1
1000	1.67	2.39	58.2	16.4
E = 50GPa, ν = 0.3, ρ = 30nm				
10	0.81	0.82	52.9	5.8
50	1.3	1.48	53.1	6.2
100	1.46	1.77	55.7	11.4
500	1.64	2.16	56.2	12.8
1000	1.67	2.16	56.9	13.7
E = 50GPa, ν = 0.47, ρ = 30nm				
10	0.81	0.76	53.6	7.2
50	1.31	1.56	50.7	1.4
100	1.48	1.97	52.7	5.4
500	1.65	2.42	53.6	7.1
1000	1.67	2.45	49.2	1.6

Table 6: Calculated E with "measured" A, for different ν, with ρ = 30 nm.

E/σ_y	Calculated A (μm^2)	"Measured" A (μm^2)	Calculated E (with "measured" A) (GPa)	% Error
E = 50GPa, ν = 0.01, ρ = 150nm				
10	0.85	0.86	57.2	14.4
50	1.32	1.41	58.5	17.1
100	1.46	1.76	57.5	15.0
500	1.64	2.42	56.5	13.1
1000	1.67	2.66	59.3	18.5
E = 50GPa, ν = 0.3, ρ = 150nm				
10	0.79	0.80	54.9	9.8
50	1.3	1.46	55.1	10.3
100	1.45	1.86	54.9	9.7
500	1.64	2.62	54.7	9.3
1000	1.67	2.63	57.6	15.2
E = 50GPa, ν = 0.47, ρ = 150nm				
10	0.79	0.85	52.1	4.2
50	1.30	1.53	52.9	5.8
100	1.47	1.79	53.7	7.3
500	1.64	2.43	49.7	0.5
1000	1.67	2.64	48.6	2.8

Table 7: Calculated E with "measured" A, for different ν, with ρ = 150 nm.